

Recovery of region boundaries of piecewise constant coefficients of an elliptic PDE from boundary data

V Kolehmainen[†], S R Arridge[‡], W R B Lionheart[§], M Vauhkonen[†] and J P Kaipio[†]

[†] Department of Applied Physics, University of Kuopio, PO Box 1627, 70211 Kuopio, Finland

[‡] Department of Computer Science, University College London, Gower Street, London WC1E 6BT, UK

[§] School of Computing and Mathematical Sciences, Oxford Brookes University, Gypsy Lane Campus, Oxford OX3 0BP, UK

Received 4 May 1999

Abstract. In this study we consider the recovery of smooth region boundaries of piecewise constant coefficients of an elliptic PDE, $-\nabla \cdot a \nabla \Phi + b \Phi = f$, from data on the exterior boundary $\partial\Omega$. The assumption made is that the values of the coefficients (a, b) are known *a priori* but the information about the geometry of the smooth region boundaries where a and b are discontinuous is missing. For the full characterization of (a, b) it is then sufficient to find the region boundaries separating different values of the coefficients. This leads to a nonlinear ill-posed inverse problem. In this study we propose a numerical algorithm that is based on the finite-element method and subdivision of the discretization elements. We formulate the forward problem as a mapping from a set of coefficients representing boundary shapes to data on $\partial\Omega$, and derive the Jacobian of this forward mapping. Then an iterative algorithm which seeks a boundary configuration minimizing the residual norm between measured and predicted data is implemented. The method is illustrated first for a general elliptic PDE and then applied to optical tomography where the goal is to find the diffusion and absorption coefficients of the object by transilluminating the object with visible or near-infrared light. Numerical test results for this specific application are given with synthetic data.

1. Introduction

Let $\Omega \in \mathbb{R}^2$ denote a bounded domain and let $\mathbf{r} = (x, y)^T \in \Omega$. We consider an elliptic PDE

$$\begin{aligned} -\nabla \cdot a \nabla \Phi + b \Phi &= f, & \mathbf{r} \in \Omega \\ c \Phi + d \frac{\partial \Phi}{\partial \nu} &= g, & \mathbf{r} \in \partial\Omega \end{aligned} \quad (1)$$

in the special case of piecewise constant coefficients a and b . Assume that Ω is divided into $L + 1$ disjoint regions A_k

$$\Omega = \cup_{k=0}^L A_k, \quad (2)$$

which are bounded by smooth closed boundary curves and have known constant coefficient values $\{a_k, b_k\}$. Let $\chi_k(\mathbf{r})$ be the characteristic function of A_k and let $C_\ell \in \Omega$ ($\ell = 1, \dots, L$) denote the smooth outer boundary of region A_ℓ . The outer boundary of the background region A_0 is $\partial\Omega$, see figure 1 for an example of the topology of the regions A_k .

Assume that $\partial\Omega$ and the values $\{a_k, b_k\}$ are known *a priori* but some of the geometrical information on the regions $\{A_k\}$ is missing. This missing information may be, for example, the

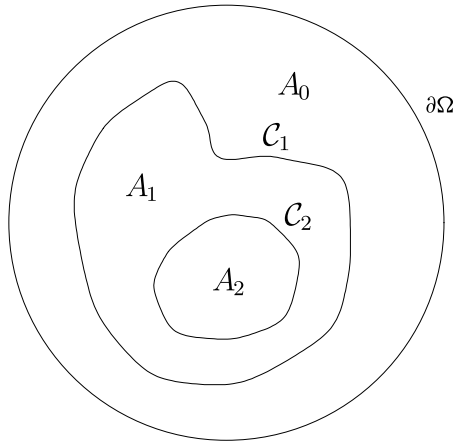


Figure 1. An example of a piecewise constant domain $\Omega = \cup_k A_k$ with constant coefficients $(a_k, b_k), k = 0, 1, 2$. The outer boundaries of regions A_1 and A_2 are denoted by C_1 and C_2 , respectively.

shapes, sizes, locations or in some cases even the number of regions. In this kind of situation it is sufficient to find the region boundaries $\{C_\ell\} \in \Omega$ ($\ell = 1, \dots, L$) for the full characterization of the coefficients (a, b) .

In this study we propose a numerical method for the recovery of the boundaries $\{C_\ell\}$ of the regions $\{A_\ell\}$ from a set of measurements $\{z_j\}$ made on the exterior boundary $\partial\Omega$ arising from a set of internal sources $\{f_j\}$ and (Dirichlet, Neumann and Robin) boundary conditions $\{g_j\}$. The forward operator, that is the projection operator $\mathcal{P}_j : a, b \mapsto z_j$ with given f_j and g_j , is denoted here by

$$z_j = \mathcal{P}_j(a, b), \quad (3)$$

where operator \mathcal{P}_j is of the form

$$\mathcal{P}_j = \mathcal{M}[\Phi_j]$$

and \mathcal{M} is some measurement operator. Furthermore, let us denote by $z := \{z_j\}$ the whole boundary data set and let

$$z = \mathcal{P}(a, b) \quad (4)$$

denote the forward operator providing the whole data set z for given sets $\{f_j\}$ and $\{g_j\}$. The goal is to approximate the shapes of the boundaries $\{C_\ell\}$ with a finite set γ of shape coefficients and then formulate the finite element method (FEM) discretization of the forward problem (4) as a mapping from the shape coefficients γ to the boundary data z . The inverse problem is then to find the representation γ of the boundary configuration when $z, \{a_k, b_k\}, \{f_j\}$ and $\{g_j\}$ are given. This inverse problem is approached as an optimization problem which seeks to minimize the residual norm between measured and predicted data. One attraction of this approach is that the dimension of the search space can be reduced in comparison with conventional pixel-wise parametrization, which potentially leads to a less ill-posed inverse problem.

The recovery of unknown boundaries of piecewise constant coefficients of a PDE is of great interest in many physical measurement techniques, useful examples include mine detection by electrostatic measurements, magnetic prospecting, crack detection from a conducting body, determination of the shape of a scattering body and electrical impedance tomography (EIT). For example, in the most elementary form of EIT the coefficients of equation (1) are $d = a = \text{conductivity}, b = f = c = 0$ and $g = \text{source current density}$. In EIT the boundary data, z , are obtained with a measurement operator \mathcal{M} which samples the potential field Φ on $\partial\Omega$ with respect to some reference potential [1, 2].

An interesting application in which boundary recovery methods have not yet been utilized is optical tomography. A widely used model for optical tomography is the diffusion approximation to the linear transport equation which is a PDE of the form (1) with the following terms: Φ is the photon density, a = diffusion, b = absorption, f is the distribution of internal sources, $c = 1$, $d = 2\vartheta a$ (ϑ is a coefficient due to the mismatch between the speed of light in the domain Ω and the surrounding medium) and g is the distribution of the boundary sources [3, 4]. In optical tomography the simplest possible measurement operator is of the form $\Gamma = \mathcal{M}[\Phi] = -a\nu \cdot \nabla \Phi$ [4, 5].

Different boundary recovery approaches have been applied successfully to elliptic PDE problems, for example, in [6–15]. All these papers contain unique ideas and give methods for solving the boundary recovery problems. However, a common feature in these papers is that they approach boundary recovery by considering some specific elliptic PDE with certain boundary conditions and data on $\partial\Omega$. In addition, most of these papers are concerned with the recovery of only one region or crack from the homogeneous background. In this study the proposed method is given in the general framework for any elliptic PDE problem. The approach we propose is suitable for the recovery of several smooth outer boundaries $\{\mathcal{C}_\ell\}$ of simply connected regions $\{A_\ell\}$ which are also allowed to be nested.

The rest of this paper is organized as follows. In the next section we give the FEM discretization of the general case of an elliptic PDE (1) and we also represent the coefficients (a, b) with respect to the set of shape coefficients γ approximating the shapes of the region boundaries $\{\mathcal{C}_\ell\}$. The forward problem is then defined as a mapping from the shape coefficients to the data: that is, $\mathcal{P} : \gamma \mapsto z$. In section 3 the inverse problem is presented as a problem of finding the region boundary configuration which optimizes the objective function representing the residual norm between measured and predicted data. The derivation of the Jacobian of the mapping $\mathcal{P} : \gamma \mapsto z$ is also given and then an iterative method for solving the inverse problem is implemented. In section 4 the proposed method is applied to optical tomography and in section 5 we give some numerical test results for this application with synthetic data. In section 6 we give conclusions and address some suggestions for future work.

2. Discretization of the elliptic PDE with the FEM

The alternatives for solving equation (1) include analytical methods, finite-difference methods, boundary element method (BEM) and FEM. Whereas analytical methods are restricted to very simple domains and finite-difference methods are awkward for arbitrary boundary shapes, the BEM and FEM offer great flexibility for arbitrary geometries and boundary shapes.

The BEM approach has been considered for boundary recovery, for example in [11–13, 15]. The BEM approach is, in a way, a natural choice since the boundaries that are discretized in this boundary integration approach are just the unknowns of the inverse problem. In addition, the use of the BEM approach is often justified over the FEM due to the lower computational cost which is of practical importance in many applications.

However, for us the FEM approach is advantageous in the sense that it allows more flexibility with respect to the coefficients. For example, in some applications the situation may be that another of the coefficients (a, b) is fixed but not piecewise constant. This kind of situation can be easily handled with the FEM approach but not with the BEM. In addition, when there are many internal boundaries the dimension of the full BEM problem rapidly reaches the dimension of the FEM problem which results in the inversion of a sparse and symmetric system matrix. Although we only consider FEM in this study with triangular elements, the method we propose can also be applied to any other elements.

In the FEM approach the domain Ω is divided into P disjoint elements $\cup_{p=1}^P \Omega_p$, joined

at D vertex nodes N_i . The solution Φ is approximated with a piecewise polynomial function $\Phi^h = \sum_{i=1}^D \phi_i \varphi_i \in \mathcal{U}^h$, where \mathcal{U}^h is a finite-dimensional subspace spanned by the basis functions φ_i ($i = 1, \dots, D$) which are chosen to have support over the elements Ω_p which have a node N_i as a vertex, that is, $\text{supp}(\varphi_i) = \cup_{p|N_i \in \Omega_p} \Omega_p$. The problem of solving Φ^h becomes one of sparse matrix inversion for which standard methods such as Cholesky decomposition or conjugate gradients are readily available.

By standard methods, equation (1) is expressed in the FEM framework as

$$(K(a) + C(b) + R)\Phi = G + F, \quad (5)$$

where the entries of the system matrices are given by

$$\begin{aligned} K_{ij} &= \int_{\Omega} a \nabla \varphi_i \cdot \nabla \varphi_j \, d\mathbf{r} \\ C_{ij} &= \int_{\Omega} b \varphi_i \varphi_j \, d\mathbf{r} \\ R_{ij} &= \int_{\partial\Omega} \frac{ac}{d} \varphi_i \varphi_j \, dS. \end{aligned} \quad (6)$$

The terms on the right-hand side of equation (5) are of the form

$$F_j = \int_{\Omega} f \varphi_j \, d\mathbf{r}, \quad G_j = \int_{\partial\Omega} \frac{a}{d} g \varphi_j \, dS. \quad (7)$$

For details see, for example, [2–4, 16].

Let us now define the piecewise constant coefficients a and b as

$$a = \sum_{k=0}^L a_k \chi_k(\mathbf{r}), \quad b = \sum_{k=0}^L b_k \chi_k(\mathbf{r}). \quad (8)$$

By substituting equation (8) into (6), we obtain the elements of K and C as

$$K_{ij} = \sum_{k=0}^L \int_{\text{supp}(\varphi_i \varphi_j) \cap A_k} a_k \nabla \varphi_i \cdot \nabla \varphi_j \, d\mathbf{r} \quad (9)$$

$$C_{ij} = \sum_{k=0}^L \int_{\text{supp}(\varphi_i \varphi_j) \cap A_k} b_k \varphi_i \varphi_j \, d\mathbf{r}. \quad (10)$$

where $\text{supp}(\varphi_i \varphi_j)$ expresses the part of the domain Ω where both basis functions φ_i and φ_j are non-zero, that is, the union of the elements that contain both nodes N_i and N_j

$$\text{supp}(\varphi_i \varphi_j) := \cup_{t|\{N_i \in \Omega_t, N_j \in \Omega_t\}} \Omega_t.$$

In this study we assume that the domains $\{A_\ell\}$ are simply connected. If the outer boundaries $\{C_\ell\}$ of the regions $\{A_\ell\}$ are sufficiently smooth, they can be approximated in the form

$$\{C_\ell(s)\} = \begin{pmatrix} x_\ell(s) \\ y_\ell(s) \end{pmatrix} = \sum_{n=1}^{N_\theta} \begin{pmatrix} \gamma_n^{x_\ell} \theta_n^x(s) \\ \gamma_n^{y_\ell} \theta_n^y(s) \end{pmatrix}, \quad \ell = 1, \dots, L \quad (11)$$

where θ_n are periodic and differentiable basis functions with period one. Let γ denote the vector of all boundary shape coefficients, that is,

$$\gamma = (\gamma_1^{x_1}, \dots, \gamma_{N_\theta}^{x_1}, \gamma_1^{y_1}, \dots, \gamma_{N_\theta}^{y_1}, \dots, \gamma_1^{x_L}, \dots, \gamma_{N_\theta}^{x_L}, \gamma_1^{y_L}, \dots, \gamma_{N_\theta}^{y_L})^T.$$

The goal is now to express the discretization of the forward model as a mapping from the boundary coefficients γ to the data z , that is, given all the boundary shape coefficients and values $\mathbf{a} = (a_0, \dots, a_\ell)^T$, $\mathbf{b} = (b_0, \dots, b_\ell)^T$, compute the data on $\partial\Omega$. The FEM implementation of this mapping is accomplished in four stages as follows:

- (i) Classification of mesh nodes as nodes inside or outside a given boundary $C_\ell(s)$. This is accomplished by counting the number of boundary crossings, λ , of a horizontal line drawn through the node $N_i = (x_i, y_i)^T$. Boundary crossings are obtained by solving the equation

$$\begin{pmatrix} x_i \\ y_i \end{pmatrix} + \lambda \begin{pmatrix} 1 \\ 0 \end{pmatrix} = \tilde{C}_\ell, \quad (12)$$

where \tilde{C}_ℓ is a finely divided polygonal approximation of $C_\ell(s)$. The decision, whether N_i is inside or outside the boundary $C_\ell(s)$, is made on the basis of the number of $\lambda > 0$ or $\lambda < 0$. If either of these is odd, N_i is inside the boundary $C_\ell(s)$. It is sufficient to carry out this test for only the nodes which are within the vertical and horizontal extent of C_ℓ . This test is known as the Jordan curve lemma and in the field of computer graphics it is also known as the ‘odd–even’ test.

- (ii) Classification of mesh elements as inside, outside or intercepted by a given region boundary $C_\ell(s)$. Let

$$B(C_\ell) := \{\Omega_m | \Omega_m \cap C_\ell \neq \emptyset\}$$

denote the set of elements intercepted by $C_\ell(s)$.

- (iii) Determination of the intersections of element edges with a given boundary $C_\ell(s)$. The goal is to find the exact intersection points $\{s_1^m, s_2^m\}$ of $C_\ell(s)$ and the element edges for each element $\Omega_m \in B(C_\ell)$. The intersection of $C_\ell(s)$ with the edge from N_i to N_j is obtained from

$$\begin{pmatrix} x_i \\ y_i \end{pmatrix} + \varepsilon \begin{pmatrix} x_j - x_i \\ y_j - y_i \end{pmatrix} = C_\ell(s) \quad (13)$$

with the condition $0 < \varepsilon \leq 1$. We use a binary search algorithm for solving equation (13). An initial search space for s is obtained from \tilde{C}_ℓ by finding the polygon points that are just outside the vertical and horizontal extent of the element edge of interest.

- (iv) Computation of the system matrices. Matrices K and C are constructed by using equations (9) and (10). Obviously, in the element set $\{\Omega_m \in B(C_\ell), \Omega_m \in \text{supp}(\varphi_i \varphi_j)\}$ we have to compute the integrals $\int \varphi_i \varphi_j \, d\mathbf{r}$ and $\int \nabla \varphi_i \cdot \nabla \varphi_j \, d\mathbf{r}$ over the intersections $A_\ell \cap \Omega_m$ and $A_r \cap \Omega_m$, see figure 2. When computing these integrals the region boundary in the intercepted element is approximated with a line drawn from $C_\ell(s_1)$ to $C_\ell(s_2)$, see the dashed line in figure 2(b). The remaining part of the element is still divided into two triangular parts by drawing a line from $C_\ell(s_1)$ to N_i (figure 2(b)). The integrals $\int \varphi_i \varphi_j \, d\mathbf{r}$ and $\int \nabla \varphi_i \cdot \nabla \varphi_j \, d\mathbf{r}$ are then computed separately over each of the three subtriangles. The integrals are mapped from subtriangles to the local element and then evaluated with a Gaussian quadrature in the local element [17].

Let $T(\gamma)$ denote the sum

$$T(\gamma) := (K(a) + C(b)). \quad (14)$$

Now the FEM equation (5) can be written in the form

$$(T(\gamma) + R)\Phi = G + F. \quad (15)$$

Equation (15) is formally solved by matrix inversion

$$\Phi = (T(\gamma) + R)^{-1}(G + F).$$

In order to relate the FEM discretization to the forward problem (3) we define the discrete forward operator for the j th source as

$$\mathcal{P}_j = \mathcal{M}_j[\Phi_j],$$

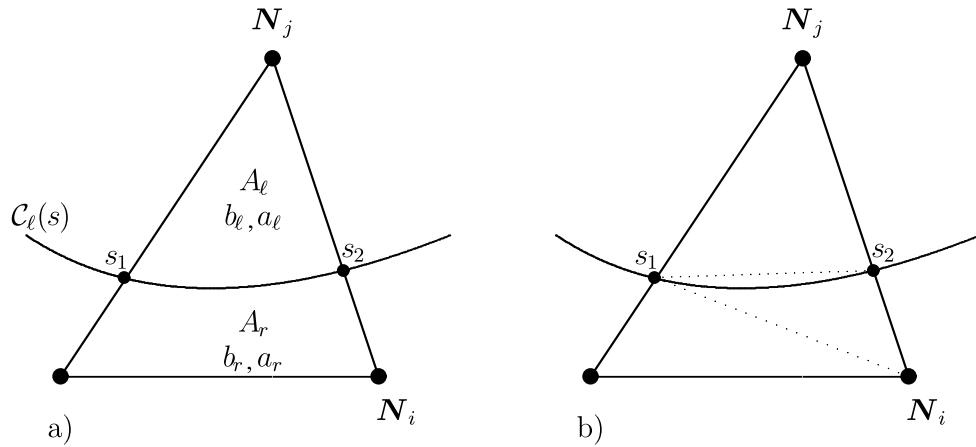


Figure 2. (a) A schematic representation of one FEM element Ω_m intercepted by the region boundary $\mathcal{C}_\ell(s)$. The pair (a_ℓ, b_ℓ) correspond to the values of the coefficients of equation (1) inside the region A_ℓ , and (a_r, b_r) are the values of the coefficients in the neighbouring region A_r , respectively. $\mathcal{C}_\ell(s_1)$ and $\mathcal{C}_\ell(s_2)$ are the intersection points of the boundary $\mathcal{C}_\ell(s)$ and the element edges. (b) The division of the Ω_m into three sub-triangles.

where \mathcal{M}_j is the discretization of the measurement operator and Φ_j is the solution to equation (15) for the j th source. Furthermore, let us denote by

$$z = \mathcal{P}(\gamma, \mathbf{a}, \mathbf{b}) \quad (16)$$

the discrete version of the forward operator (4) which gives the vector $z = (z_1, z_2, \dots, z_S)^T$ of samples of the whole data set for all S sources.

3. Inverse problem

If we denote by z_{meas} the vector of measurements for a given set of sources, the cost functional to be minimized can be written as

$$\Xi(\gamma) = \|z_{\text{meas}} - \mathcal{P}(\gamma, \mathbf{a}, \mathbf{b})\|_2^2. \quad (17)$$

The inverse problem consists of finding the boundary configuration which minimizes the cost functional (17), that is

$$\text{find } \gamma^* \text{ such that } \Xi(\gamma^*) = \min \|z_{\text{meas}} - \mathcal{P}(\gamma^*, \mathbf{a}, \mathbf{b})\|_2^2. \quad (18)$$

A natural way to solve this nonlinear problem is to use Newton-type methods where we seek a zero of $\Xi'(\gamma)$ by an iterative method using Taylor expansion around the current estimate, γ_k . This leads to an algorithm

$$\gamma_{k+1} = \gamma_k + (\Xi''(\gamma_k))^{-1} \Xi'(\gamma_k) \quad (19)$$

where $\Xi'(\gamma_k) = J_k^T (z_{\text{meas}} - \mathcal{P}(\gamma_k, \mathbf{a}, \mathbf{b}))$ and the inverse of $\Xi''(\gamma_k)$ is usually approximated with $(J_k^T J_k)^{-1}$. However, in our case the Jacobian matrices J_k are usually ill-conditioned and therefore we stabilize the algorithm using the Levenberg–Marquardt method

$$\gamma_{k+1} = \gamma_k + (J_k^T J_k + \lambda I)^{-1} J_k^T (z_{\text{meas}} - \mathcal{P}(\gamma_k, \mathbf{a}, \mathbf{b})), \quad (20)$$

where λ is a control parameter.

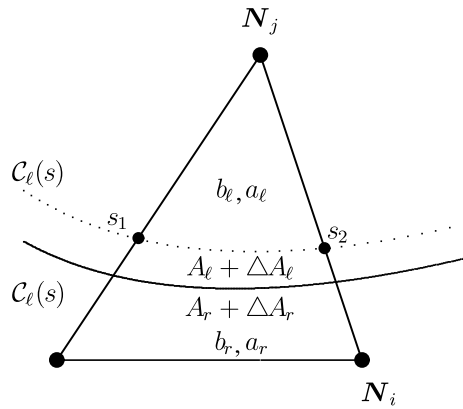


Figure 3. Perturbation in the boundary C_ℓ . The perturbed curve is of the form $\tilde{C}_\ell = C_\ell + (\epsilon\theta_n^x, 0)^T$ when perturbation is in the x -coordinate and $\tilde{C}_\ell = C_\ell + (0, \epsilon\theta_n^y)^T$ when it is in the y -coordinate. In this simple case we have $\Delta A_\ell = \delta A_\ell^+ - 0$ and $\Delta A_r = 0 - \delta A_r^-$.

The Jacobian matrix

$$J = \frac{\partial \mathcal{P}(\gamma, \mathbf{a}, \mathbf{b})}{\partial \gamma}$$

is obtained as follows. By differentiating equation (15) with respect to the boundary coefficient $\gamma_n^{\alpha_\ell}$ (α is either x or y), we obtain

$$T \frac{\partial \Phi}{\partial \gamma_n^{\alpha_\ell}} = - \frac{\partial T}{\partial \gamma_n^{\alpha_\ell}} \Phi, \tag{21}$$

where we have assumed that the derivatives of R , G and F with respect to the boundary coefficients are zero.

By definition

$$\frac{\partial T}{\partial \gamma_n^{\alpha_\ell}} = \lim_{\epsilon \rightarrow 0} \frac{T(\gamma + \epsilon \theta_n^\alpha(s)) - T(\gamma)}{\epsilon} \tag{22}$$

where ϵ is a arbitrarily small perturbation in the basis function $\theta_n^\alpha(s)$ of either $x_\ell(s)$ or $y_\ell(s)$. Perturbation in one parameter $\gamma_n^{\alpha_\ell}$ changes the region configuration from $\{A_k\}$ to $\{\tilde{A}_k\}$. Let $\tilde{\chi}_k(\mathbf{r})$ denote the characteristic functions of the perturbed regions \tilde{A}_k . Furthermore, let us define the signed differences δA_k^+ and δA_k^- as

$$\begin{aligned} \delta A_k^+ &= (\tilde{A}_k \setminus A_k) \cap \tilde{A}_k \\ \delta A_k^- &= (\tilde{A}_k \setminus A_k) \cap A_k. \end{aligned} \tag{23}$$

By using equation (23) we can write the relation

$$\tilde{A}_k = A_k + \Delta A_k, \tag{24}$$

where

$$\Delta A_k = \delta A_k^+ - \delta A_k^-.$$

See figure 3 for a simple example of the perturbed region.

By using equations (9), (10) and (14) we obtain the matrix elements in equation (22) as

$$\begin{aligned} \left(\frac{\partial T}{\partial \gamma_n^{\alpha_\ell}} \right)_{ij} &= \lim_{\epsilon \rightarrow 0} \frac{1}{\epsilon} \left\{ \left(\sum_{k=0}^L \int_{\text{supp}(\varphi_i \varphi_j) \cap \tilde{A}_k} a_k \nabla \varphi_i(\mathbf{r}) \cdot \nabla \varphi_j(\mathbf{r}) \, d\mathbf{r} \right. \right. \\ &\quad \left. \left. + \sum_{k=0}^L \int_{\text{supp}(\varphi_i \varphi_j) \cap \tilde{A}_k} b_k \varphi_i(\mathbf{r}) \varphi_j(\mathbf{r}) \, d\mathbf{r} \right) \right\} \end{aligned}$$

$$\begin{aligned}
& - \left(\sum_{k=0}^L \int_{\text{supp}(\varphi_i \varphi_j) \cap A_k} a_k \nabla \varphi_i(\mathbf{r}) \cdot \nabla \varphi_j(\mathbf{r}) \, d\mathbf{r} \right. \\
& \left. + \sum_{k=0}^L \int_{\text{supp}(\varphi_i \varphi_j) \cap A_k} b_k \varphi_i(\mathbf{r}) \varphi_j(\mathbf{r}) \, d\mathbf{r} \right) \Big\} \\
& = \lim_{\epsilon \rightarrow 0} \frac{1}{\epsilon} \left\{ (b_\ell - b_r) \sum_{m | \Omega_m \in \text{supp}(\varphi_i \varphi_j)} \int_{\Delta A_\ell \cap \Omega_m} \varphi_i(\mathbf{r}) \varphi_j(\mathbf{r}) \, d\mathbf{r} \right. \\
& \left. + (a_\ell - a_r) \sum_{m | \Omega_m \in \text{supp}(\varphi_i \varphi_j)} \int_{\Delta A_\ell \cap \Omega_m} \nabla \varphi_i(\mathbf{r}) \cdot \nabla \varphi_j(\mathbf{r}) \, d\mathbf{r} \right\}, \quad (25)
\end{aligned}$$

where (a_ℓ, b_ℓ) are the coefficient values in the region A_ℓ , which has C_ℓ as the outer boundary, and (a_r, b_r) are the values in the (outer) neighbouring region A_r , which has C_ℓ as the inner boundary.

Next, let us consider the evaluation of equation (25) in simplified notation. The problem is the evaluation of expressions of the form

$$\lim_{\epsilon \rightarrow 0} \frac{1}{\epsilon} \sum_m \iint_{\Delta A_\ell \cap \Omega_m} f(x, y) \, dx \, dy, \quad (26)$$

where $f(x, y)$ is either $\varphi_i \varphi_j$ or $\nabla \varphi_i \cdot \nabla \varphi_j$. The area of integration depends on the perturbation ϵ , as follows.

We define a new positively oriented coordinate system (p, s) where s is the positively oriented parametrization of the closed curve C_ℓ , and p multiplies a perturbation vector pointing outward from the region A_ℓ

$$\begin{pmatrix} p \\ s \end{pmatrix} \mapsto \begin{pmatrix} x_\ell(s) \\ y_\ell(s) \end{pmatrix} + p \begin{pmatrix} \xi(s) \\ \eta(s) \end{pmatrix} = \begin{pmatrix} x(s) \\ y(s) \end{pmatrix}. \quad (27)$$

The boundary \tilde{C}_ℓ of the perturbed region \tilde{A}_ℓ can be expressed in the new coordinate system as

$$s \mapsto \begin{pmatrix} x_\ell(s) \\ y_\ell(s) \end{pmatrix} + \epsilon \begin{pmatrix} \xi(s) \\ \eta(s) \end{pmatrix} = \tilde{C}_\ell(s).$$

By utilizing the coordinate transformation (27) in equation (26) we obtain the form

$$\lim_{\epsilon \rightarrow 0} \frac{1}{\epsilon} \int_{p=0}^{\epsilon} \int_{s=s_1}^{s_2} f(x, y) \frac{\partial(x, y)}{\partial(p, s)} \, ds \, dp = \frac{d}{d\epsilon} \Big|_{\epsilon=0} \int_{p=0}^{\epsilon} \int_{s=s_1}^{s_2} f(x, y) \frac{\partial(x, y)}{\partial(p, s)} \, ds \, dp. \quad (28)$$

In the new coordinate system the region of integration is the rectangular strip $[s_1 \, s_2] \times [0 \, \epsilon]$ in each of the elements Ω_m . The Jacobian determinant $\frac{\partial(x, y)}{\partial(p, s)}$ is obtained as

$$\left| \begin{pmatrix} \frac{\partial x}{\partial p} \\ \frac{\partial y}{\partial p} \end{pmatrix}_s = \begin{pmatrix} \xi \\ \eta \end{pmatrix} \quad \begin{pmatrix} \frac{\partial x}{\partial s} \\ \frac{\partial y}{\partial s} \end{pmatrix}_p = \begin{pmatrix} \dot{x} + p\dot{\xi} \\ \dot{y} + p\dot{\eta} \end{pmatrix} \right|$$

and by evaluating this, we have

$$\frac{d}{d\epsilon} \Big|_{\epsilon=0} \int_{p=0}^{\epsilon} \int_{s=s_1}^{s_2} f(x, y) (\xi(\dot{y} + p\dot{\eta}) - \eta(\dot{x} + p\dot{\xi})) \, ds \, dp. \quad (29)$$

By evaluating equation (29) and using (28) we get the result

$$\lim_{\epsilon \rightarrow 0} \frac{1}{\epsilon} \int_{p=0}^{\epsilon} \int_{s=s_1}^{s_2} f(x, y) \frac{\partial(x, y)}{\partial(p, s)} \, ds \, dp = \int_{s=s_1}^{s_2} f(x, y) (\xi \dot{y} - \eta \dot{x}) \, ds. \quad (30)$$

The final results for the elements of the matrices $\frac{\partial T}{\partial \gamma_n^{x_\ell}}$ and $\frac{\partial T}{\partial \gamma_n^{y_\ell}}$ are obtained by applying the result (30) to equation (25). When differentiating with respect to $\gamma_n^{x_\ell}$, that is perturbing $\theta_n^x(s)$, we have $\xi = \theta_n^x(s)$, $\eta = 0$ and the elements of $\frac{\partial T}{\partial \gamma_n^{x_\ell}}$ are obtained as

$$\left(\frac{\partial T}{\partial \gamma_n^{x_\ell}}\right)_{ij} = \sum_{m|\Omega_m \in B(\mathcal{C}_\ell) \cap \text{supp}(\varphi_i \varphi_j)} \left[(b_\ell - b_r) \int_{s_1}^{s_2} \varphi_i \varphi_j \dot{y}_\ell(s) \theta_n^x(s) ds + (a_\ell - a_r) \int_{s_1}^{s_2} \nabla \varphi_i \cdot \nabla \varphi_j \dot{y}_\ell(s) \theta_n^x(s) ds \right]. \quad (31)$$

Correspondingly, when differentiating with respect to $\gamma_n^{y_\ell}$ we have $\eta = \theta_n^y(s)$, $\xi = 0$ and the elements of $\frac{\partial T}{\partial \gamma_n^{y_\ell}}$ are obtained as

$$\left(\frac{\partial T}{\partial \gamma_n^{y_\ell}}\right)_{ij} = \sum_{m|\Omega_m \in B(\mathcal{C}_\ell) \cap \text{supp}(\varphi_i \varphi_j)} \left[-(b_\ell - b_r) \int_{s_1}^{s_2} \varphi_i \varphi_j \dot{x}_\ell(s) \theta_n^y(s) ds - (a_\ell - a_r) \int_{s_1}^{s_2} \nabla \varphi_i \cdot \nabla \varphi_j \dot{x}_\ell(s) \theta_n^y(s) ds \right]. \quad (32)$$

The limits of integration s_1 and s_2 in equations (31) and (32) are the values of the curve parameter in the intersection points of the element edges and boundary curve \mathcal{C}_ℓ in each element Ω_m , see figure 3.

By solving equation (21) for the j th source

$$\frac{\partial \Phi_j}{\partial \gamma_n^{\alpha_\ell}} = -T^{-1} \frac{\partial T}{\partial \gamma_n^{\alpha_\ell}} \Phi_j$$

and applying the discrete measurement operator \mathcal{M}_j , we obtain the vector

$$\rho_{j,m} = \mathcal{M}_j \left[\frac{\partial \Phi_j}{\partial \gamma_n^{\alpha_\ell}} \right] \quad (33)$$

which is the j th block of the m th column corresponding to differentiation with respect to the coefficient $\gamma_n^{\alpha_\ell}$ in the Jacobian J . Here we have assumed that the measurement operator \mathcal{M} is independent of the configuration of the region boundaries $\{\mathcal{C}_\ell\}$. The Jacobian can be also constructed efficiently by utilizing the adjoint method [5].

4. Application to optical tomography

By optical tomography we mean the use of visible or near-infrared light in the wavelength range ~ 700 – 1000 nm, to probe highly scattering media in order to derive images of the optical properties of the object. Of the potential applications, the most attention has been received by applications in medical imaging, such as the detection of cancerous tumours in breast tissue and the monitoring of infant brain tissue oxygenation levels [18].

In optical tomography, the measurement system consists of S optic fibres placed on the source positions $\varepsilon_j \in \partial\Omega$ and M optic fibres placed in the measurement positions $\zeta_i \in \partial\Omega$. The methods of data acquisition in optical tomography can be divided into frequency domain and time-resolved methods. In the frequency domain methods, light from a radio-frequency modulated source is usually guided via the optic fibres to one source location ε_j at a time, and the phase shift and modulation amplitude of the transmitted light is measured at the measurement locations ζ_i , $i = 1, \dots, M$ by using the optic fibres and light-sensitive detectors [19]. This process is then repeated for all source locations ε_j , $j = 1, \dots, S$. Correspondingly, in the time-resolved methods an ultra-short input pulse (~ 10 ps) is usually triggered to one source location ζ_i at a time, and the impulse response function $\Gamma_{i,j}(t)$ of the object is measured at

the detector locations ε_j , $j = 1, \dots, S$. Due to the multiple scattering events occurring in the highly scattering medium, different photons arrive at the detector at different times, and this causes the response function $\Gamma(t)$ to be spread over a time period of several nanoseconds in width [3, 18, 20–23].

The inverse problem in optical tomography is to reconstruct maps of the optical properties of the object Ω based on the set of boundary data $\{\Gamma_{i,j}\}$. The image reconstruction can be carried out by using the whole spatio-temporal data set, or alternatively, the reconstruction can be carried out by using some temporal integral transform of $\Gamma_{i,j}(t)$ as the data [24, 25]. In the results of this study we consider recovery of the region boundaries by using only the simplest data type, namely the DC intensity

$$E_{i,j} = \Gamma_{i,j}(\omega = 0) = \int_0^\infty \Gamma_{i,j}(t) dt. \quad (34)$$

The use of alternative data types complicates the presentation of the method, so it is not discussed further here, although it is certainly of interest in optical tomography and may lead to better performance of our method [5, 24, 25].

Although light transport in scattering media is properly modelled with the radiative transfer equation (RTE), most of the current approaches to optical tomography use the diffusion approximation to the RTE as the forward model. In the case of the DC-intensity (34) the diffusion approximation is a PDE of the same form as (1) where Φ is the photon density,

$$a = 1/(3(b + e'_s)) \quad (35)$$

is the diffusion coefficient, b the absorption coefficient, $e'_s = (1 - \bar{\Theta})e_s$ the reduced scattering coefficient, e_s the scattering coefficient, $\bar{\Theta}$ the mean cosine of the scattering phase function and the rest of the coefficients in equation (1) are as given in section 1 [4, 5]. In cases other than DC intensity the diffusion approximation contains an additional term with respect to equation (1). In the frequency domain case the additional term is $\frac{i\omega}{c}\Phi$, resulting in a complex field. In the time domain case the corresponding PDE is parabolic, but the data types of interest can be obtained by recursively solving a set of elliptic equations [5]. In either case, these additional terms do not affect the crucial parts of the boundary estimation algorithm given above. The diffusion approximation has been validated to give reasonable accuracy in scattering dominated media ($e'_s \gg b$). For further details on the diffusion approximation to the RTE, see [5, 26–33].

In the diffusion approximation model sources are usually modelled as either a collimated point source which is placed inside the domain Ω one mean free path from $\partial\Omega$, or as a diffuse photon source on $\partial\Omega$ [4]. In the case of a collimated point source we have a non-zero distribution of internal sources $f_j \neq 0$, and we set the boundary sources $g_j = 0$ in equation (1). In the case of diffuse boundary sources, which is the source model we use in this study, we set $f_j = 0$ and

$$g_j = \begin{cases} \Gamma_{s_j} & \mathbf{r} \in \varepsilon_j \\ 0 & \mathbf{r} \in \partial\Omega \setminus \varepsilon_j. \end{cases}$$

The relation between the response function Γ and the photon density Φ is of the form

$$\Gamma_{i,j} = -a(\zeta_i)\boldsymbol{\nu} \cdot \nabla\Phi_j(\zeta_i) \quad (36)$$

in the diffusion approximation model. For details on the models of optical tomography and on the limitations of different models, see [5, 31, 34] and references therein.

5. Numerical results

In this section we consider some numerical examples of the proposed method applied to optical tomography. In order to be able to implement the numerical method given in sections 2 and 3

to the model of optical tomography which was given in section 4, we have to choose the basis functions $\theta_n^x(s)$ and $\theta_n^y(s)$ for the curve parametrization given in equation (11). In this study we use basis functions of the form

$$\begin{aligned}\theta_1^\alpha(s) &= 1 \\ \theta_n^\alpha(s) &= \sin\left(2\pi\frac{n}{2}(s+\phi^s)\right), \quad n = 2, 4, 6, \dots \\ \theta_n^\alpha(s) &= \cos\left(2\pi\left(\frac{n}{2}-1\right)(s+\phi^s)\right), \quad n = 3, 5, 7, \dots,\end{aligned}\quad (37)$$

where ϕ^s is the phase of the curve parameter and α denotes either x or y . Before applying the boundary estimation method with this parametrization of the curve \mathcal{C}_ℓ we have to fix the phase of the curve parameter s in equation (11). Basically, the same curve \mathcal{C}_ℓ can be represented with an infinite variety of different shape coefficients γ by adjusting the phase ϕ^s with infinitesimal changes on the interval $]0, 1[$. If the phase is not fixed when utilizing the boundary estimation method, we obtain a one-dimensional nullspace \mathcal{N}_ℓ per curve \mathcal{C}_ℓ when computing the Jacobian matrix. This null space is due to this phase ambiguity. In this study the phase is fixed by a very simple method, that is, by using unequal amounts of sin and cos terms, i.e., we just set the number of basis functions N_θ to an even number. A clear advantage of this phase-fixing method is that we do not necessarily have to know any interior point $\mathbf{r}_0 \in A_\ell$ when we utilize it for fixing the phase ϕ^s .

The synthetic measurement system we use in this study consists of 16 sources and 16 detectors placed in equiangular positions with the order $\varepsilon_1, \zeta_1, \varepsilon_2, \zeta_2, \dots, \varepsilon_{16}, \zeta_{16}$ on the boundary $\partial\Omega$ of a circular domain Ω which has a radius of 25 mm. In the inverse computations the domain Ω was discretized to $P = 6776$ triangular elements Ω_p and the number of nodes in this mesh was $D = 3517$. In the formulation of the numerical method given in sections 2 and 3 the conditions for the nodal basis functions are that φ_i is piecewise differentiable and has support $\text{supp}(\varphi_i) = \cup_{p|N_i \in \Omega_p} \Omega_p$. In this study we use the first-order basis functions φ_i .

The simulations were carried out by using the logarithm of the DC intensity $z_{i,j} = \log E_{i,j}$ as the data. In the discrete mode the forward solution for the DC intensity (34) is obtained by solving Φ_j from the FEM discretization of an elliptic PDE in equation (15) [5, 25], and then applying $\mathbf{E}_j = \mathcal{M}[\Phi_j] = D\Phi_j$, where D is a linear discrete operator

$$D_{in} = \begin{cases} \frac{1}{2\vartheta} \varphi_n(\zeta_i), & \text{if node } i \in \Omega_{\zeta_i}, \\ 0, & \text{otherwise} \end{cases}, \quad i = 1, \dots, M \quad n = 1, \dots, P. \quad (38)$$

Equation (38) is obtained by using equation (36) and the boundary condition in equation (1) [5]. The Jacobian for the data $z_j = \log(\mathbf{E}_j)$ corresponding to the j th source is obtained by utilizing equations (33), (38) and $\frac{d}{dx} \log(g(x)) = \frac{g'(x)}{g(x)}$.

In the following simulations the values of the coefficients for the diffusion approximation were chosen from the range of interest in medical imaging [5]. For the absorption coefficient b we used values in the range $0.025\text{--}0.05 \text{ mm}^{-1}$, for the scattering coefficient e_s we used values in the range $20\text{--}40 \text{ mm}^{-1}$ and for the mean cosine we used a typical value $\bar{\Theta} = 0.9$ which indicates strongly forward biased scattering [4]. The values of diffusion coefficient a were computed using equation (35).

The number of photons collected in each measurement was assumed to be 10^4 for each source and random noise which follows the statistical noise model given in [35] was added to the synthetic data. The mesh we used for the generation of the synthetic data consisted of $P = 8600$ triangular elements and $D = 4429$ nodes. In the data generation we used a greater number of trigonometric basis functions $\theta_n^\alpha(s)$ than in the inverse computations.

In the following simulations the inverse problem was solved by using the Levenberg–Marquardt method (20). The stabilization parameter λ and the number of iterations were

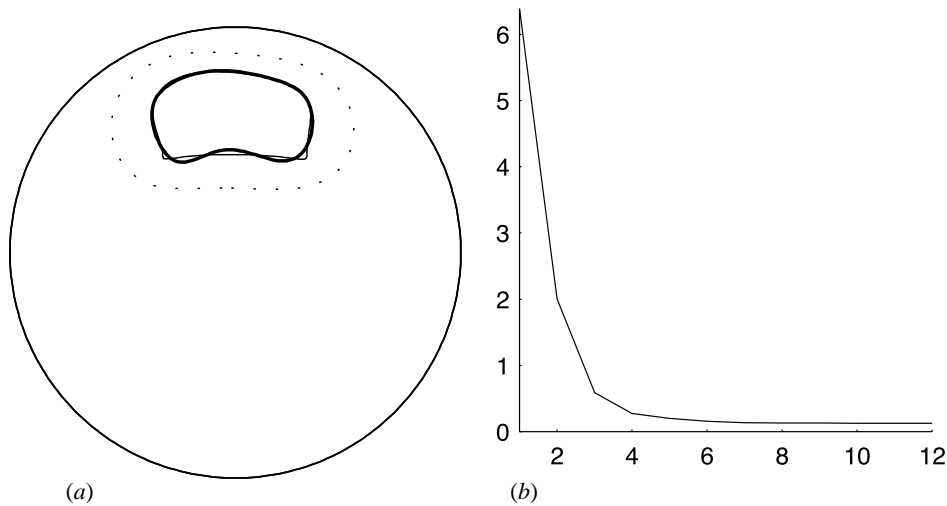


Figure 4. (a) Test case with a single perturbation A_1 . Parameter values are $(b_0, b_1, e_{s_0}, e_{s_1}) = (0.025, 0.05, 20, 40) \text{ mm}^{-1}$. The bold line denotes the true boundary, the thin line the reconstructed boundary and the dotted line denotes the initial estimate. The dimension of the search space is 16. (b) The relative data error percentage $\|z_{\text{meas}}\|^{-1} \|z_{\text{meas}} - \mathcal{P}(\gamma_k, \mathbf{a}, \mathbf{b})\| \cdot 100\%$ versus iteration index k .

chosen manually by performing a large number of different tests. The initial estimate γ_0 was obtained by drawing an arbitrary polygon relatively near the true $\{\mathcal{C}_\ell\}$ and then solving the coefficients γ_0 by using a least squares fit to the set of polygon points. In the inverse computations we used $N_\theta = 8$ basis functions of the form (37) for the curve representation (11).

Results of the simulations are shown in figures 4(a)–7(a). The true boundary is represented by a bold line, the reconstructed boundary by a thin line and the initial estimate for the iteration by a dotted line. Figures 4(b)–7(b) contain plots of the relative data error percentage $\|z_{\text{meas}}\|^{-1} \|z_{\text{meas}} - \mathcal{P}(\gamma_k, \mathbf{a}, \mathbf{b})\|$ versus iteration index k .

The result for the first test case is shown in figure 4(a). The values of the parameters are as follows: in the background A_0 the values are $b_0 = 0.025 \text{ mm}^{-1}$ and $e_{s_0} = 20 \text{ mm}^{-1}$, and in the perturbation A_1 values of b and e_s reach twice those of the background, i.e. $b_1 = 0.05 \text{ mm}^{-1}$ and $e_{s_1} = 40 \text{ mm}^{-1}$. In this test case the stabilization parameter was $\lambda = 0.2$. As can be seen this simple perturbation A_1 , which has good contrast with respect to the background in both parameters, can be recovered with good accuracy from noisy data. The relative data error (%) versus iteration index k is shown in figure 4(b).

Results for the second test case are shown in figure 5. Parameter values are as follows: in the background A_0 the values are $b_0 = 0.025 \text{ mm}^{-1}$ and $e_{s_0} = 20 \text{ mm}^{-1}$. The first target, A_1 , which is located up and left from the centre of Ω , has contrast in both parameters ($b_1 = 0.05 \text{ mm}^{-1}$, $e_{s_1} = 40 \text{ mm}^{-1}$) with respect to the background. The second target, A_2 , which is located below the centre of Ω , has contrast only in b with the values ($b_2 = 0.05 \text{ mm}^{-1}$, $e_{s_2} = 20 \text{ mm}^{-1}$), and the third target, A_3 , has contrast only in e_s with the values ($b_3 = 0.025 \text{ mm}^{-1}$, $e_{s_3} = 40 \text{ mm}^{-1}$), respectively. In the reconstruction shown in figure 5 the stabilization parameter was $\lambda = 0.2$. As can be seen, all three regions are found with good accuracy, and it seems that the small differences in the contrast do not have much effect on the accuracy obtained in the recovery of the different regions. It is also worth noting

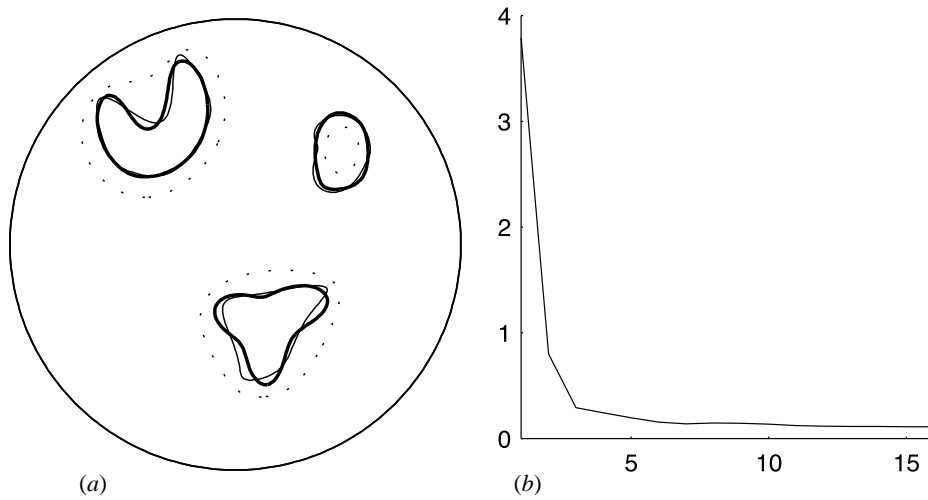


Figure 5. (a) Test case with three perturbations. Target A_1 is located up and left from the centre of Ω , A_2 is located below the centre of Ω and A_3 is located right of centre. Parameter values are $(b_0, b_1, b_2, b_3, e_{s_0}, e_{s_1}, e_{s_2}, e_{s_3}) = (0.025, 0.05, 0.05, 0.025, 20, 40, 20, 40) \text{ mm}^{-1}$. The bold lines denote the true boundaries, the thin lines the reconstructed boundaries and the dotted lines denote the initial estimate. The dimension of the search space is 48. (b) The relative data error $\|z_{\text{meas}}\|^{-1} \|z_{\text{meas}} - \mathcal{P}(\gamma_k, \mathbf{a}, \mathbf{b})\| \cdot 100\%$ versus k .

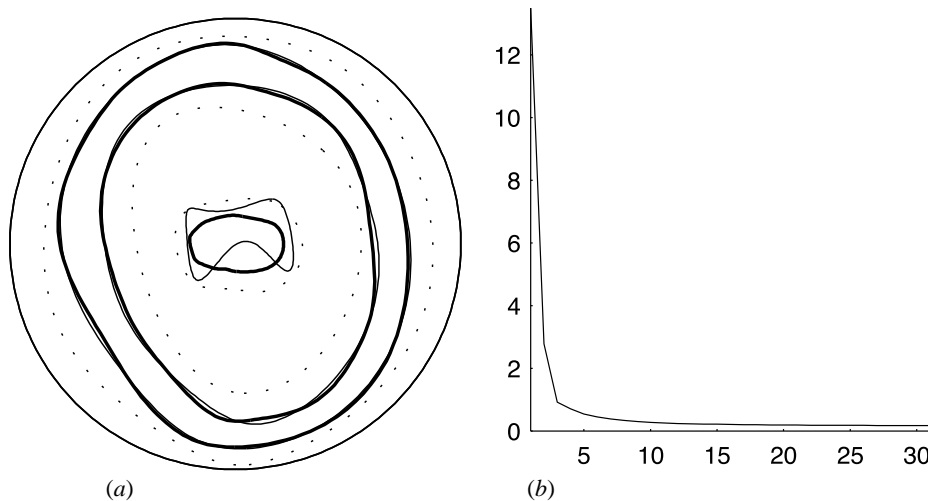


Figure 6. (a) Test case with three nested boundaries. Subdomains A_0 – A_3 are in respective order from $\partial\Omega$ towards the centre of Ω . Parameter values are $(b_0, b_1, b_2, b_3, e_{s_0}, e_{s_1}, e_{s_2}, e_{s_3}) = (0.025, 0.05, 0.025, 0.03, 20, 40, 20, 30) \text{ mm}^{-1}$. The bold lines denote the true boundaries, the thin lines the reconstructed boundaries and the dotted lines denote the initial estimate. The dimension of the search space is 48. (b) The relative data error $\|z_{\text{meas}}\|^{-1} \|z_{\text{meas}} - \mathcal{P}(\gamma_k, \mathbf{a}, \mathbf{b})\| \cdot 100\%$ versus k .

that in the region A_3 the reconstruction is initiated inside the true boundary \mathcal{C}_3 .

Results for the third test case, which has some resemblance to a cross section of an infant's head, are shown in figure 6. The four nested regions A_k , $k = 0, 1, 2, 3$ of this simulated phantom are in respective order from the boundary $\partial\Omega$ towards the centre of the domain Ω .

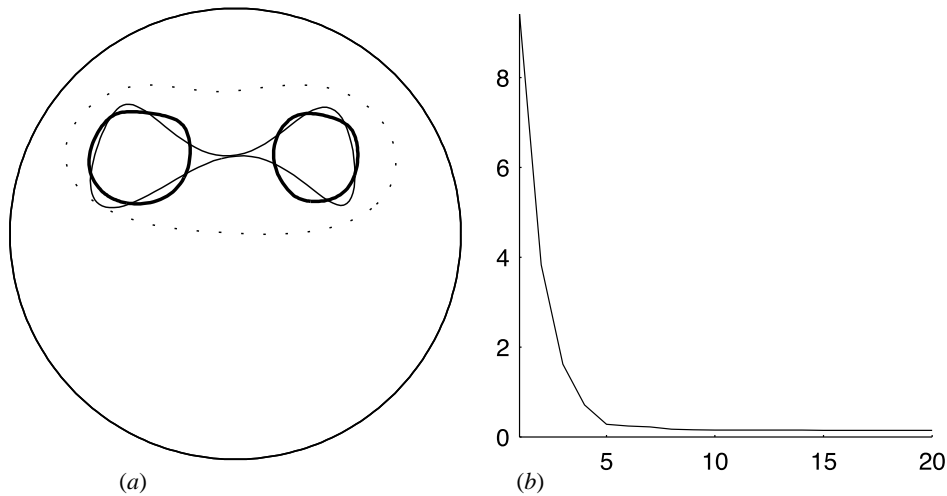


Figure 7. (a) The true phantom has two perturbation regions A_1 and A_2 . Parameter values are $(b_0, b_1, b_2, e_{s_0}, e_{s_1}, e_{s_2}) = (0.025, 0.05, 0.05, 20, 40, 40) \text{ mm}^{-1}$. The bold lines denote the true boundaries, the thin line the reconstructed boundary and the dotted line denotes the initial estimate. The dimension of the search space is 16. (b) The relative data error $\|z_{\text{meas}}\|^{-1} \|z_{\text{meas}} - \mathcal{P}(\gamma_k, a, b)\| \cdot 100\%$ versus k .

The values of coefficients are as follows: $b_0 = 0.025 \text{ mm}^{-1}$, $e_{s_0} = 20 \text{ mm}^{-1}$, $b_1 = 0.05 \text{ mm}^{-1}$, $e_{s_1} = 40 \text{ mm}^{-1}$, $b_2 = 0.025 \text{ mm}^{-1}$, $e_{s_2} = 20 \text{ mm}^{-1}$, $b_3 = 0.03 \text{ mm}^{-1}$ and $e_{s_3} = 30 \text{ mm}^{-1}$. In figure 6 the stabilization parameter was $\lambda = 1.4$. In this case, the boundaries \mathcal{C}_1 and \mathcal{C}_2 , that is the ‘skin–skull’ and ‘skull–brain’ interfaces, were found with good accuracy whereas the innermost region boundary \mathcal{C}_3 was found with poor accuracy. This can be expected since the amount of light propagating to the centre of Ω is extraordinarily small due to the highly damping circular region A_1 .

The method proposed relies on the assumption that we have some initial estimate for the boundaries. In the results shown in figures 4–6 we assumed that the number and approximate locations of the regions $\{A_\ell\}$ were known *a priori* when constructing the initial estimates. In these cases the boundaries $\{\mathcal{C}_\ell\}$ were found with good accuracy and the convergence of the method was fast. In the fourth test case, shown in figure 7, we assumed that the approximate location of the perturbation was known but we made an error in the number of the perturbations. In figure 7 the true distribution has two perturbed regions A_1 and A_2 with the same contrast ($b_{1,2} = 0.05 \text{ mm}^{-1}$, $e_{s_{1,2}} = 40 \text{ mm}^{-1}$) with respect to the background values ($b_0 = 0.025 \text{ mm}^{-1}$, $e_{s_0} = 20 \text{ mm}^{-1}$). As an initial estimate we used a single perturbation surrounding both regions A_1 and A_2 . In the reconstruction shown in figure 7 the stabilization parameter was $\lambda = 5$. Based on this result it seems that it could be possible, in some cases, to take the splitting and merging of the regions into account by utilizing some supplementary decision algorithm which uses, for example, some minimum distance or crossing-point criteria to decide whether the regions should be split or merged.

We also conducted several test cases in which we tested the effects of a poor initial estimate. In these tests we made large errors in the location of the target in the initial estimates. Based on these tests it seems that the proposed method does not perform well when the initial estimate is very far from the true boundaries. The poor performance of the method in these cases appeared as unpractically slow convergence and stability problems. However, in most situations we have reasonable good *a priori* information about the anatomy of the object, and

thus we can construct reasonably good initial estimates.

It is worth noting that the implementation of the method is easier when one is considering of equation of the form $-\nabla \cdot a \nabla \Phi = f$ and using first-order basis functions φ_j . In these cases the integration $\int \nabla \varphi_i \cdot \nabla \varphi_j \, d\mathbf{r}$ over one element $\Omega_m \in \text{supp}(\varphi_i \varphi_j)$ in equation (9) does not have to be computed separately over the three split parts of the element, but is instead obtained as

$$\frac{a_\ell S_\ell + a_r S_r}{S_\ell + S_r} \int_{\Omega_m} \nabla \varphi_i \cdot \nabla \varphi_j \, d\mathbf{r},$$

where $S_\ell = A_\ell \cap \Omega_m$ and $S_\ell \cup S_r = \Omega_m$, see figure 2.

6. Conclusions

In this paper we proposed a new numerical method for the recovery of several internal region boundaries of piecewise constant coefficients of an elliptic PDE. The proposed method is based on the series expansion approximation of the smooth region boundaries and on the FEM. The proposed method led to an inverse problem which was solved iteratively using the Levenberg–Marquardt method. The proposed method was formulated in a general framework for elliptic PDEs, and then applied to optical tomography which is a field in which boundary recovery methods have not been utilized previously. Numerical results were given with synthetic data. Based on the test results it seems that the overall performance of the method is promising. A weakness of the method was highlighted by the fact that there are convergence and stability problems in cases in which the initial estimates were a long way from the true boundaries. In these cases it would be possible to look for a good initial estimate by first performing a normal pixelwise reconstruction, or alternatively, by recovering the approximate locations and sizes of the regions by reconstructing only a few Fourier coefficients in the first stage.

We made the following relatively weak assumptions regarding the topology in the proposed method: (1) boundaries are closed and sufficiently smooth; (2) the regions enclosed by the boundaries are simply connected. In this study these boundaries were approximated with separate Fourier series for both coordinates of each of the boundary curves. A minor drawback of the curve approximation chosen is that it does not include assumption (2) as a constraint. This caused stability problems in the test cases where the initial estimate was a long way from the true situation. In these cases the Levenberg–Marquardt method exhibited the tendency to produce self-intersecting boundaries. One possible solution to these problems with convergence and constraints on admissible solutions would be to use some non-trivial, object-based prior information for the boundary shapes. Such a method would be the subspace regularization method [2]. In addition, regularization can be expected to improve the ill-posedness of the problem.

The proposed method is flexible with respect to the curve approximation. The minimal conditions for the curve approximation are periodicity and differentiability, and for the regions the minimal requirement is that they possess simple connections. Otherwise, the choice of the curve approximation depends on the topological conditions of the application and is the free choice of the user. For example, if we can assume that the boundaries enclose star-like regions we can use a simpler curve approximation. Naturally, if we were still using the same amount of basis functions θ_n , the number of parameters would be reduced to half that in the current version and would lead to a less ill-posed problem.

In this study we restricted ourselves to the case in which the values of the piecewise constant coefficients were known, and the only unknown information was on the geometry of the boundaries where the coefficients are discontinuous. The method can also be expanded

to the more complicated case in which the values of the coefficients are also considered as unknown quantities. However, this will lead to a more ill-posed inverse problem. Other aspects that could be investigated are the dependence of the performance on the varying number of measurements and the use of different data types such as frequency domain or time-dependent measurements.

Acknowledgments

This work was supported by the Vilho, Yrjö and Kalle Väisälä Fund, the Saastamoinen Foundation, the Savo Foundation for Advanced Technology, the British Council and the Academy of Finland.

References

- [1] Somersalo E, Cheney M and Isaacson D 1992 Existence and uniqueness for electrode models for electric current computed tomography *SIAM J. Appl. Math.* **52** 1023–40
- [2] Vauhkonen M, Vadasz D, Karjalainen P A, Somersalo E and Kaipio J P 1998 Tikhonov regularization and prior information in electrical impedance tomography *IEEE Trans. Med. Imaging* **17** 285–93
- [3] Arridge S R, Schweiger M, Hiraoka M and Delpy D T 1993 A finite element approach for modelling photon transport in tissue *Med. Phys.* **20** 299–309
- [4] Schweiger M, Arridge S R, Hiraoka M and Delpy D T 1995 The finite element model for the propagation of light in scattering media: boundary and source conditions *Med. Phys.* **22** 1779–92
- [5] Arridge S R 1999 Optical tomography in medical imaging *Inverse Problems* **15** R41–93
- [6] Hettlich F and Rundell W 1996 Iterative methods for the reconstruction of an inverse potential problem *Inverse Problems* **12** 251–66
- [7] Hettlich F and Rundell W 1998 The determination of a discontinuity in a conductivity from a single boundary measurement *Inverse Problems* **14** 67–82
- [8] Hettlich F and Rundell W 1997 Recovery of the support of a source term in an elliptic differential equation *Inverse Problems* **13** 959–76
- [9] Alessandrini G and Rosset E 1998 The inverse conductivity problem with one measurement: bounds on the size of the unknown object *SIAM J. Appl. Math.* **58** 1060–71
- [10] Alessandrini G and Rondi L 1998 Stable determination of a crack in a planar inhomogeneous conductor *SIAM J. Math. Anal.* **30** 326–40
- [11] Santosa F, Alessandrini G, Beretta E and Vessella S 1995 Stability in crack determination from electrostatic measurements at the boundary—a numerical investigation *Inverse Problems* **11** L17–24
- [12] Chahine G L, Duraiswami R and Sarkar K 1997 Boundary element techniques for efficient 2-d and 3-d electrical impedance tomography *Chem. Engng Sci.* **52** 2185–96
- [13] Bonnet M 1995 Bie and material differentiation applied to the formulation of obstacle inverse problems *Engng Anal. Bound. Elem.* **15** 121–36
- [14] Lesselier D, Litman A and Santosa F 1998 Reconstruction of a two-dimensional binary obstacle by controlled evolution of a level-set *Inverse Problems* **14** 685–706
- [15] Santosa F, Kaup P G and Vogelius M 1996 Method of imaging corrosion damage in thin plates from electrostatic data *Inverse Problems* **12** 279–93
- [16] Brenner S C and Scott L R 1994 *The Mathematical Theory of Finite Element Methods* (Berlin: Springer)
- [17] Cuvelier C and Segal A 1986 *Finite Element Methods and Navier–Stokes Equations* (Dordrecht: Reidel)
- [18] Arridge S R and Schweiger M 1998 A general framework for iterative reconstruction algorithms in optical tomography, using a finite element method *Computational Radiology and Imaging: Therapy and Diagnosis (IMA Volumes in Mathematics and its Applications vol 110)* ed C Borgers and F Natterer (Berlin: Springer) at press
- [19] Jiang H, Paulsen K D, Osterberg U L, Pogue B W and Patterson M S 1995 Optical image reconstruction using frequency-domain data: simulations and experiments *J. Opt. Soc. Am.* **13** 253–66
- [20] Delpy D T, Cope M, van der Zee P, Arridge S R, Wray S and Wyatt J 1988 Estimation of optical pathlength through tissue from direct time of flight measurement *Phys. Med. Biol.* **33** 1433–42
- [21] Model R, Ortl M, Walzel M and Hünlich R 1997 Reconstruction algorithm for near-infrared imaging in turbid media by means of time-domain data *J. Opt. Soc. Am.* **14** 313–24

- [22] Saquib S S, Hanson K M and Cunningham G S 1997 *Proc. SPIE* **3034** 369–80
- [23] Colak S B, Papaioannou D G, 't Hooft G W, van der Mark M B, Schomberg H, Paasschens J C J, Melissen J B M and van Asten N A A J 1997 Tomographic image reconstruction from optical projections in light-diffusing media *Appl. Opt.* **36** 180–213
- [24] Schweiger M and Arridge S R 1997 Optimal data types in optical tomography *Proc IPMI 97: Information Processing in Medical Imaging (Lecture Notes in Computer Science vol 1230)* (Berlin: Springer) pp 71–84
- [25] Arridge S R and Schweiger M 1995 Direct calculation of the moments of the distribution of photon time of flight in tissue with a finite-element method *Appl. Opt.* **34** 2683–7
- [26] Chandrasekhar S 1950 *Radiative Transfer* (London: Oxford University Press)
- [27] Davison B 1957 *Neutron Transport Theory* (Oxford: Oxford University Press)
- [28] Weinberg A M and Wigner E P 1958 *The Physical Theory of Neutron Chain Reactors* (Chicago, IL: University of Chicago Press)
- [29] Case M C and Zweifel P F 1967 *Linear Transport Theory* (New York: Addison Wesley)
- [30] Duderstadt J J and Martin W R 1979 *Transport Theory* (New York: Wiley)
- [31] Dorn O 1998 A transport–backtransport method for optical tomography *Inverse Problems* **14** 1107–30
- [32] Ackroyd R T 1997 *Finite Element Methods for Particle Transport: Applications to Reactor and Radiation Physics* (Taunton: Research Studies Press)
- [33] Ishimaru A 1978 *Wave Propagation and Scattering in Random Media* vol 1 (New York: Academic)
- [34] Gryazin Y A, Klibanov M V and Lucas T R 1999 Imaging the diffusion coefficient in a parabolic inverse problem in optical tomography *Inverse Problems* **15** 373–97
- [35] Arridge S R, Hiraoka M and Schweiger M 1995 Statistical basis for the determination of optical pathlength in tissue *Phys. Med. Biol.* **40** 1539–58